

A Model for the Oxidative Pyrolysis of Wood

Chris Lautenberger[‡] and Carlos Fernandez-Pello

Department of Mechanical Engineering

University of California, Berkeley

Berkeley, CA 94720, USA

A generalized pyrolysis model is applied to simulate the oxidative pyrolysis of white pine slabs irradiated under nonflaming conditions. Conservation equations for gaseous and solid mass, energy, species, and gaseous momentum (Darcy's law approximation) inside the decomposing solid are solved to calculate profiles of temperature, mass fractions, and pressure inside the decomposing wood. The condensed-phase consists of four species, and the gas that fills the voids inside the decomposing solid consists of seven species. Four heterogeneous (gas/solid) reactions and two homogeneous (gas/gas) reactions are included. Diffusion of oxygen from the ambient into the decomposing solid and its effect on local reactions occurring therein is explicitly modeled. A genetic algorithm is used to extract the required material properties from experimental data at 40 kW/m² and ambient oxygen concentrations of 0%, 10.5% and 21%. Next, experiments conducted at 25 kW/m² irradiance are simulated to assess the model's predictive capabilities for conditions not included in the property estimation process. The optimized model calculations for mass loss rate, surface temperature, and in-depth temperatures reproduce well the experimental data, including the experimentally observed increase in temperature and mass loss rate with increasing oxygen concentration.

Keywords: Wood; pyrolysis; oxidative pyrolysis; charring; char oxidation

[‡] Corresponding author. Tel: 510-643-0178; Fax: 510-642-1850; Email: clauten@me.berkeley.edu.

Nomenclature

Letters

A	Condensed-phase species A (reactant)
b	Exponent in Eq. 16
B	Condensed-phase species B (product)
c	Specific heat capacity
E	Activation energy
h	Enthalpy
h_c	Convective heat transfer coefficient
k	Thermal conductivity
K	Number of heterogeneous reactions or permeability
ℓ	Index of homogeneous gas phase reaction
L	Number of homogeneous gas phase reactions
\dot{m}''	Mass flux
M	Molecular weight or number of condensed phase species
N	Number of gaseous species
n	Exponent (reaction order, O ₂ sensitivity, property temperature dependence)
p	Exponent in Eq. 16
P	Pressure
q	Exponent in Eq. 16
\dot{q}''	Heat flux
\dot{Q}'''	Heat generation per unit volume
R	Universal gas constant
t	Time
T	Temperature
X	Volume fraction
y	Yield
Y	Mass fraction
z	Distance
Z	Pre-exponential factor

Greek Symbols

γ	Radiative conductivity parameter
δ	Thickness or Kronecker delta
ε	Emissivity
κ	Radiative absorption coefficient
ν	Viscosity (μ/ρ) or reaction stoichiometry coefficient (Eq. 8)
ρ	Bulk density in a vacuum
ψ	Porosity
$\dot{\omega}'''$	Reaction rate

Subscripts

0	Initial
∞	Ambient
Σ	See Eq. 10
<i>ash</i>	Ash
<i>cop</i>	Char oxidation products
<i>d</i>	Destruction
<i>dw</i>	Dry wood
<i>e</i>	External
<i>f</i>	Formation
<i>g</i>	Gaseous
H ₂ O	Water vapor
<i>i</i>	Condensed phase species <i>i</i>
<i>j</i>	Gaseous species <i>j</i>
<i>k</i>	Reaction index
<i>ℓ</i>	Homogeneous reaction index
<i>op</i>	Oxidative pyrolysate
O ₂	Oxygen
<i>r</i>	Radiative or reference
<i>s</i>	Solid
<i>tp</i>	Thermal pyrolysate
<i>v</i>	Volatiles
<i>ww</i>	Wet wood

Superscripts

°	At time <i>t</i>
---	------------------

1. Introduction

During a compartment fire, combustible solids may be exposed to oxygen concentrations ranging from the ambient value to near zero when a surface is covered by a diffusion flame. The presence or absence of oxygen can affect solid materials' decomposition kinetics and thermodynamics to different degrees. For example, the thermal stability of polymethylmethacrylate (PMMA) is relatively insensitive to oxygen [1] when compared with polypropylene (PP) and polyethylene (PE) which both show a marked decrease in thermal stability as oxygen concentration is increased [2]. During wood pyrolysis in an inert environment, the volatile formation process is endothermic [3], but in oxidative environments such as air, oxidative reactions occurring near the surface (such as char oxidation) are exothermic and can lead to visible glowing.

In thermogravimetry, small samples of material with mass on the order of a few milligrams are heated in an atmosphere having a known (often linearly increasing) temperature, and the resultant mass loss is measured with a high precision scale. The effect of oxygen concentration on thermogravimetric experiments has been widely investigated, and models for oxygen-sensitive decomposition have been developed [4, 5]. However, by design there are negligible gradients of temperature and species concentrations in thermogravimetric experiments, and the oxygen concentration that the degrading sample "feels" is approximated as the ambient value. Consequently, lumped models based on transient ordinary differential equations can be applied with good results.

In comparison, significant gradients of temperature and species are usually present during the pyrolysis of a solid fuel slab (for example, in a Cone Calorimeter experiment). Near the exposed surface, oxygen concentrations may approach ambient values; however, there may be little or no oxygen present at in-depth locations. Due to these spatial variations in temperature and species concentrations, which can only be simulated by solving partial differential equations, modeling oxidative pyrolysis of a solid fuel slab is more complex than simulating a lumped thermogravimetric experiment.

Despite the potentially significant effect of oxidative pyrolysis on a material's overall reaction to fire, modeling the effect of oxygen concentration on the decomposition of a thermally stimulated solid fuel slab has been infrequently explored. Reaction kinetics and thermodynamics of polymer oxidative pyrolysis have been directly related to the free-stream oxygen concentration [6, 7]. However, the oxygen concentration at the exposed surface may be reduced due to blowing, and this effect cannot be captured with this modeling approach.

Although many models have been presented for the pyrolysis of wood slabs, rarely are exothermic oxidative reactions explicitly considered. For example, Shen *et al.* [8] recently modeled the pyrolysis of several different species of wet wood using three parallel reactions. Although they simulated Cone Calorimeter experiments conducted in air, all three reactions were modeled as endothermic so oxidative pyrolysis was not explicitly considered. Oxidative pyrolysis of wood has been simulated by including the effect of exothermic reactions in the exposed face boundary condition [9, 10], but oxidative reactions do not necessarily occur only immediately at the surface.

This paper presents a comprehensive model for the oxidative pyrolysis of wood slabs. A novel feature is that conservation equations are solved for each gaseous species inside the decomposing wood. Rather than relating reaction kinetics and thermodynamics to the freestream oxygen concentration, they are related to the local oxygen concentration inside the decomposing wood. This is made possible by explicitly calculating the diffusion of oxygen from the ambient into the pores of a decomposing wood slab where it may participate in oxidative pyrolysis. Both heterogeneous (gas/solid) and homogeneous (gas/gas) reactions inside the decomposing solid (not just at its surface) are considered. The model's predictive capabilities are assessed by comparing its calculations to experimental data for the oxidative pyrolysis of white pine [11, 12].

2. Formulation of generalized charring pyrolysis model

The modeling presented in this paper is a specific application of a generalized pyrolysis model developed previously by the authors. Although this model is described in detail elsewhere [13, 14], the main equations are presented below for completeness.

2.1. Governing equations

A slab of thermally decomposing wood is modeled as consisting of a condensed phase (wood, char, ash) coupled to a gas phase (oxygen, nitrogen, water vapor, pyrolysate, etc.). The gas phase outside of the decomposing wood slab (the exterior ambient) is not modeled, so any discussion of the gas phase refers to the gases inside the pores or voids that form in decomposing wood. The following assumptions are invoked:

- One-dimensional behavior

- Each condensed-phase species has well-defined properties: bulk density, specific heat capacity, effective thermal conductivity, emissivity, in-depth radiation absorption coefficient, permeability, porosity
- Thermal conductivity and specific heat capacity of each condensed phase species vary as $k(T) = k_0(T/T_r)^{n_k}$ and $c(T) = c_0(T/T_r)^{n_c}$ where T_r is a reference temperature, k_0 and c_0 are the values of k and c , and the exponents n_k and n_c specify whether k or c increase or decrease with T
- Radiation heat transfer across pores is accounted for by adding a contribution to the effective thermal conductivity that increases as T^3 , i.e. $k_{r,i} = \gamma_i \sigma T^3$
- Averaged properties appearing in the conservation equations (denoted by overbars) are calculated by appropriate mass or volume weightings
- All gaseous species have equal diffusion coefficients and specific heat capacities (independent of temperature)
- Darcian pressure-driven flow through porous media (Stokes flow)
- Unit Schmidt number ($\nu = D$)
- Gas-phase and condensed-phase are in thermal equilibrium
- No shrinkage or swelling (volume change) occurs

The conservation equations (derived in Ref. [13]) that result from the above assumptions are given as Eqs. 1 - 7:

Condensed phase mass conservation:

$$\frac{\partial \bar{\rho}}{\partial t} = -\dot{\omega}_{fg}''' \quad (1)$$

Condensed phase species conservation:

$$\frac{\partial(\bar{\rho}Y_i)}{\partial t} = \dot{\omega}_{fi}'' - \dot{\omega}_{di}'' \quad (2)$$

Gas phase mass conservation:

$$\frac{\partial(\rho_g \bar{\nu})}{\partial t} + \frac{\partial \dot{m}''}{\partial z} = \dot{\omega}_{fg}'' \quad (3)$$

Gas phase species conservation:

$$\frac{\partial(\rho_g \bar{\nu} Y_j)}{\partial t} + \frac{\partial(\dot{m}'' Y_j)}{\partial z} = -\frac{\partial \dot{j}_j''}{\partial z} + \dot{\omega}_{fi}'' - \dot{\omega}_{dj}'' \quad (4)$$

Condensed phase energy conservation:

$$\frac{\partial(\bar{\rho}h)}{\partial t} + \frac{\partial(\dot{m}'' h_g)}{\partial z} = -\frac{\partial \dot{q}''}{\partial z} + \dot{Q}'' + \sum_{i=1}^M (\dot{\omega}_{fi}'' - \dot{\omega}_{di}'') h_i \quad (5)$$

Gas phase energy conservation:

$$T_g = T \quad (\text{thermal equilibrium}) \quad (6)$$

Gas phase momentum conservation (assumes Darcian flow):

$$\frac{\partial}{\partial t} \left(\frac{P \bar{M} \bar{\nu}}{RT_g} \right) = \frac{\partial}{\partial z} \left(\frac{\bar{K}}{\nu} \frac{\partial P}{\partial z} \right) + \dot{\omega}_{fg}'' \quad (7)$$

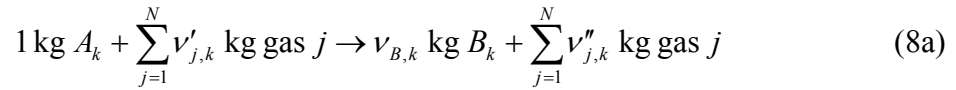
In Eq. 4, the diffusive mass flux is calculated from Fick's law as $\dot{j}_j'' = -\bar{\nu} \rho_g D \frac{\partial Y_j}{\partial z}$, and in

Eq. 5 the conductive heat flux is calculated from Fourier's law as $\dot{q}'' = -\bar{k} \frac{\partial T}{\partial z}$. Note that

Y_i is the mass of condensed phase species i divided by the total mass of all condensed phase species, and Y_j is the mass of gaseous species j divided by the mass of all gaseous species. Similarly, $\dot{\omega}_{fi}'''$ is the formation rate of condensed phase species i , and $\dot{\omega}_{di}'''$ is the destruction rate of condensed phase species i . The analogous gas-phase quantities are $\dot{\omega}_{fj}'''$ and $\dot{\omega}_{dj}'''$. The temperature-dependent diffusion coefficient D in Eq. 4 is obtained from Chapman-Enskog theory [15].

2.2. Reactions and source terms

There are K heterogeneous (solid/gas) reactions, and individual condensed phase reactions are indicated by the index k . Heterogeneous reaction k converts condensed-phase species A_k to condensed phase species B_k plus gases according to the general stoichiometry:



$$v_{B,k} = \frac{\rho_{B_k}}{\rho_{A_k}} \quad (8b)$$

$$v'_{j,k} = -(1 - v_{B,k}) \min(y_{s,j,k}, 0) \quad (8c)$$

$$v''_{j,k} = (1 - v_{B,k}) \max(y_{s,j,k}, 0) \quad (8d)$$

Here, $y_{s,j,k}$ is a user-specified N by K species yield matrix that controls the values of $v'_{j,k}$ and $v''_{j,k}$. Its entries are positive for the formation of gaseous species and negative for the

consumption of gaseous species. The destruction rate of condensed phase species A_k by reaction k is calculated as:

$$\dot{\omega}_{dA_k}'' = \left(\frac{\bar{\rho}Y_{A_k}}{(\bar{\rho}Y_{A_k})_\Sigma} \right)^{n_k} (\bar{\rho}Y_{A_k})_\Sigma Z_k \exp\left(-\frac{E_k}{RT}\right) \quad (\text{for } n_{O_2,k} = 0) \quad (9a)$$

$$\dot{\omega}_{dA_k}'' = \left(\frac{\bar{\rho}Y_{A_k}}{(\bar{\rho}Y_{A_k})_\Sigma} \right)^{n_k} (\bar{\rho}Y_{A_k})_\Sigma \left[(1 + Y_{O_2})^{n_{O_2,k}} - 1 \right] Z_k \exp\left(-\frac{E_k}{RT}\right) \quad (\text{for } n_{O_2,k} \neq 0) \quad (9b)$$

$$(\bar{\rho}Y_i)_\Sigma \equiv (\bar{\rho}Y_i)|_{t=0} + \int_0^t \dot{\omega}_{fi}''(\tau) d\tau \quad (9c)$$

In Eq. 9, parameter $n_{O_2,k}$ controls a reaction's oxygen sensitivity, and the oxygen mass fraction (Y_{O_2}) is the local value inside the decomposing solid determined by solution of Eq. 4. Combining Eqs. 8 and 9, it can be seen that the volumetric formation rate of condensed phase species B_k by reaction k is:

$$\dot{\omega}_{fB_k}'' = \nu_{B,k} \dot{\omega}_{dA_k}'' = \frac{\rho_{B_k}}{\rho_{A_k}} \dot{\omega}_{dA_k}'' \quad (11)$$

Similarly, the formation rate of all gases due to consumption of condensed phase species A_k by reaction k is:

$$\dot{\omega}_{fg_k}'' = (1 - \nu_{B,k}) \dot{\omega}_{dA_k}'' = \left(1 - \frac{\rho_{B_k}}{\rho_{A_k}} \right) \dot{\omega}_{dA_k}'' \quad (12)$$

It also follows from Eqs. 8 and 9 that the formation and destruction rates of gaseous species j by reaction k are:

$$\dot{\omega}_{fj,k}'' = \nu_{j,k}'' \dot{\omega}_{dA_k}'' = \dot{\omega}_{fg,k}'' \max(y_{s,j,k}, 0) \quad (13a)$$

$$\dot{\omega}_{dj,k}'' = \nu'_{j,k} \dot{\omega}_{dA_k}'' = -\dot{\omega}_{fg,k}'' \min(y_{s,j,k}, 0) \quad (13b)$$

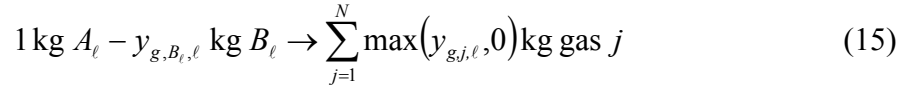
The volumetric rate of heat release or absorption to the solid phase due to reaction k is calculated as:

$$\dot{Q}_{s,k}'' = -\dot{\omega}_{fB_k}'' \Delta H_{s,k} - \dot{\omega}_{fg_k}'' \Delta H_{v,k} \quad (14)$$

where $\Delta H_{s,k}$ and $\Delta H_{v,k}$ are the heats of reaction associated respectively with the formation of condensed-phase species and gas-phase species by reaction k .

Homogeneous gas-phase reactions inside the decomposing wood are also accounted for. Just as there are K condensed phase reactions and individual condensed phase reactions are indicated by the index k , there are L homogeneous gas phase reactions and individual reactions are indicated by the index ℓ . Each homogeneous gas phase reaction ℓ converts two gas phase reactants (A_ℓ and B_ℓ) to gaseous products.

The stoichiometry of homogeneous gas phase reactions is expressed here on a mass basis as:



In Equation 15, $y_{g,j,\ell}$ is a user-specified N by L “homogeneous gaseous species yield matrix”, analogous to the gaseous species yield matrix ($y_{s,j,k}$) discussed earlier with reference to heterogeneous reactions. The physical meaning of the entries in $y_{g,j,\ell}$ is the mass of gaseous species j produced by reaction ℓ (for positive entries) or consumed by reaction ℓ (for negative entries) per unit mass of gaseous species A_ℓ consumed. Eq. 15 has

been written assuming that $y_{g,A_\ell,\ell} = -1$, i.e. the reaction is normalized to 1 kg of gaseous species A_ℓ .

The reaction rate of the ℓ^{th} homogeneous gas phase reaction is the destruction rate of gas phase species A_ℓ :

$$r_\ell = \dot{\omega}_{dA_\ell}''' = [A_\ell]^{p_\ell} [B_\ell]^{q_\ell} T^{b_\ell} Z_\ell \bar{\nu} \exp\left(-\frac{E_\ell}{RT_g}\right) \quad (16)$$

In Equation 16, $[A]$ denotes the molar gas-phase concentration of gaseous species A :

$$[A] = \frac{\rho_g Y_A}{M_A} \quad (17)$$

The creation or destruction of gaseous species j by homogeneous gaseous reaction ℓ is calculated from the homogeneous gaseous species yield matrix ($y_{g,j,\ell}$) as:

$$\dot{\omega}_{g,j,\ell}''' = r_\ell y_{g,j,\ell} = \dot{\omega}_{dA_\ell}''' y_{g,j,\ell} \quad (18)$$

The volumetric rate of heat release to the gas phase by homogeneous gaseous reaction ℓ is:

$$\dot{Q}_{g,\ell}''' = -\dot{\omega}_{dA_\ell}''' \Delta H_\ell \quad (19)$$

where ΔH_ℓ is the heat of reaction associated with homogeneous gas phase reaction ℓ .

Since multiple reactions (both heterogeneous and homogeneous) may occur, the source terms appearing in the governing equations must be determined by summing over all reactions. The total formation rate of all gases from the condensed phase is:

$$\dot{\omega}_{fg}''' = \sum_{k=1}^K \dot{\omega}_{fg_k}''' \quad (20)$$

Similarly, the total formation/destruction rates of condensed phase species i and gas-phase species j are obtained as:

$$\dot{\omega}_{di}''' = \sum_{k=1}^K \delta_{i,A_k} \dot{\omega}_{dA_k}''' \quad \text{where } \delta_{i,A_k} = \begin{cases} 1 & \text{if } i = A_k \\ 0 & \text{if } i \neq A_k \end{cases} \quad (21a)$$

$$\dot{\omega}_{fi}''' = \sum_{k=1}^K \delta_{i,B_k} \dot{\omega}_{fB_k}''' \quad \text{where } \delta_{i,B_k} = \begin{cases} 1 & \text{if } i = B_k \\ 0 & \text{if } i \neq B_k \end{cases} \quad (21b)$$

$$\dot{\omega}_{dj}''' = \sum_{k=1}^K \dot{\omega}_{dj,k}''' + \sum_{\ell=1}^L \max(\dot{\omega}_{g,j,\ell}''', 0) \quad (22a)$$

$$\dot{\omega}_{fj}''' = \sum_{k=1}^K \dot{\omega}_{fj,k}''' - \sum_{\ell=1}^L \min(\dot{\omega}_{g,j,\ell}''', 0) \quad (22b)$$

The total heat source/sink \dot{Q}''' appearing in the condensed phase energy conservation equation is calculated by summing Eq. 14 and Eq. 19 over all reactions:

$$\dot{Q}''' = \sum_{k=1}^K \dot{Q}_{s,k}''' + \sum_{\ell=1}^L \dot{Q}_{g,\ell}''' \quad (23)$$

Due to the assumption of thermal equilibrium between the gaseous and the condensed phases (Eq. 6), any heat release due to homogeneous gas-phase reactions (Eq. 19) is added to the condensed phase energy conservation equation source term \dot{Q}''' . In a “two temperature” model where thermal equilibrium between the condensed phase and the gas phase is not assumed, the heat release due to homogeneous gas-phase reactions (right most term in Eq. 23) should be added to the source term appearing in the conservation of gas-phase energy equation.

2.3. Solution methodology

When discretized, the above equations yield a system of coupled algebraic equations that are solved numerically. The recommendations of Patankar [16] are followed closely. Due to the nonlinearity introduced by the source terms and temperature-dependent thermophysical properties, a fully-implicit formulation is adopted for solution of all equations. The condensed phase energy conservation equation, gas-phase species conservation equation, and gas-phase momentum conservation equation are solved using a computationally efficient tridiagonal matrix algorithm (TDMA). The condensed phase mass and condensed phase species conservation equations are solved with a customized fully implicit solver that uses overrelaxation to prevent divergence. Source terms are split into positive and negative components to ensure physically realistic results and prevent negative mass fractions or densities from occurring [16]. Newton iteration is used to extract the temperature from the weighted enthalpy and the condensed phase species mass fractions. Additional details are given in Ref. [13]. Initial and boundary conditions are presented in Section 3.2.

3. Simulation of white pine oxidative pyrolysis

In this section, the charring pyrolysis model presented above in general form is applied to simulate the oxidative pyrolysis of white pine slabs irradiated under nonflaming conditions. Model calculations are compared with the experimental data of Ohlemiller, Kashiwagi, and Werner [11, 12] who studied the effects of ambient oxygen concentration on the nonflaming gasification of irradiated white pine slabs. In the experiments, white pine cubes 3.8 cm on edge (density of 380 kg/m^3 and moisture

content of 5% by mass) were irradiated at 25 kW/m² and 40 kW/m² in oxygen concentrations of 0%, 10.5%, and 21% (normal air) by volume.

Fig. 1 illustrates some of the key measurements that make this set of experiments particularly interesting from a modeling perspective. Fig. 1a shows that in the 40 kW/m² experiments, the mass loss rate measured in air is approximately double that measured in nitrogen. The effect of oxidative exothermic reactions is also evident in Fig. 1b, where it can be seen that the surface temperature of the sample tested in air was approximately 150 °C greater than that of the sample tested in nitrogen. In addition to the mass loss rate and surface temperature measurements shown in Fig. 1, in-depth thermocouple temperature measurements are also reported [12].

3.1 Modeling approach

The model described in Section 2 is presented in general form, meaning that it could potentially be used to simulate many different charring materials or experimental configurations. What differentiates one material or experiment from another is the material's thermophysical properties and reaction mechanism (sometimes called material properties) as well as the initial and boundary conditions that describe the experimental conditions. Postulating a basic modeling approach (number of species to track, reaction mechanism, physics to include in the simulation) and then determining the required model input parameters is one of the most challenging aspects of pyrolysis modeling. In this work, a previously developed genetic algorithm optimization method [17, 18] is used to extract the required input parameters from the experimental data at one heat flux level (40 kW/m²). Experimental data from the second heat flux level (25 kW/m²) are used to

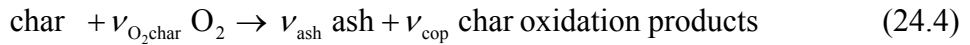
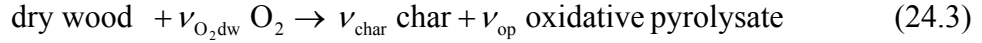
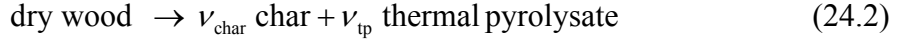
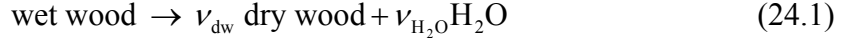
assess the model's predictive capabilities under experimental conditions that were not included in input parameter optimization.

In the modeling approach applied here, white pine is simulated as consisting of four condensed-phase species, numbered as follows: 1) wet wood, 2) dry wood, 3) char, and 4) ash. The bulk density of each species is constant, but thermal conductivities and specific heat capacities are temperature dependent. Each species is permitted to have a different surface emissivity to account for blackening of the wood as it chars. All condensed-phase species are opaque (no diathermancy) and radiation heat transfer across pores is accounted for in the char and ash species (which have high porosities). Permeability of all species is held fixed at 10^{-10} m^2 because scoping simulations indicated that permeability had a negligible effect on the calculated mass loss rate and temperature profiles (the experimental measurements against which the model calculations are judged).

In addition to the four condensed-phase species, seven gaseous species are tracked: 1) thermal pyrolysate, 2) nitrogen, 3) water vapor, 4) oxygen, 5) oxidative pyrolysate, 6) char oxidation products, and 7) pyrolysate oxidation products. It is assumed that all species have identical specific heat capacities (1000 J/kg-K) and equal mass diffusivities. As mentioned earlier, unit Schmidt number ($\nu = D$) and thermal equilibrium between the condensed and gaseous phases are assumed.

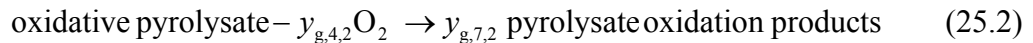
Four condensed phase (heterogeneous) reactions are considered. Reaction 1 converts wet wood to dry wood and water vapor. Reaction 2 is the anaerobic conversion of dry wood to char plus thermal pyrolysate. Reaction 3 also converts dry wood to char, but consumes oxygen in the process to produce oxidative pyrolysate. Finally, reaction 4

converts char to ash, consuming oxygen in the process, and produces char oxidation products. This reaction mechanism can be summarized as:



The first (drying) reaction is modeled after Atreya [19]. Per Eq. 8, the ν coefficients in Eq. 24 are related to bulk density ratios and the heterogeneous gaseous species yield matrix discussed earlier, e.g. $\nu_{\text{dw}} = \rho_{\text{dw}} / \rho_{\text{ww}}$ and $\nu_{\text{op}} = (1 - \rho_{\text{char}} / \rho_{\text{ww}}) y_{s,5,3}$.

Two homogeneous (gas-gas) reactions are also considered. They are oxidation of thermal pyrolysate to form pyrolysate oxidation products, and oxidation of oxidative pyrolysate to form pyrolysate oxidation products:



In Eq. 25, $y_{g,j,\ell}$ is the homogeneous gaseous species yield matrix discussed earlier.

The reaction mechanism in Eq. 24 and Eq. 25 differs from the conventional modeling approach wherein char oxidation is viewed as a heterogeneous process occurring at (or near) the surface of a decomposing solid [9, 10]. In the present work, oxidative exothermic reactions, including both heterogeneous reactions (Eq. 24.3 and Eq. 24.4) and homogeneous gas-gas reactions (Eq. 25.1 and 25.2), are permitted to occur in-depth.

Considerable simplifications are inherent in the reaction mechanisms embodied in Equations 24 and 25. Gaseous “pseudo” or “surrogate” species are used to represent complex gas mixtures. For example, a single gaseous species called “char oxidation products” is used to represent the gases that form via heterogeneous char oxidation (Equation 24.4). In reality, these gases may include a mixture of CO, CO₂, H₂O, unburnt hydrocarbons, etc., but since very little is known about the actual composition of these gases, they are tracked in the model by a single surrogate species. Another approximation stems from the simultaneous formation of “char” by the thermal pyrolysis of dry wood (Equation 24.2) and the oxidation of dry wood (Equation 24.3). In reality, the chemical composition of char formed by thermal pyrolysis of wood is not expected to be the same as that formed by oxidation of the wood. However, the complexity of the above mechanism would be significantly increased if a second char species (such as oxidative char) were added.

Similarly, thermal pyrolysate (which forms in the absence of oxygen from the pyrolysis of dry wood) and oxidative pyrolysate (which forms by the oxidation of dry wood) are chemically distinct mixtures of species that are tracked by a single surrogate species. Thus, it is expected that their combustion products would be different. However, it can be seen from Equations 25.1 and 25.2 that the oxidation of both species produces pyrolysate oxidation products. Again, this approximation is invoked to reduce the number of species that must be tracked.

3.2 Initial and boundary conditions representing experimental configuration

Initial and boundary conditions are specified to simulate the experiments described in Ref. [12]. The initial temperature, pressure, gaseous species mass fractions, and condensed phase species are initially uniform throughout the thickness of the solid:

$$(\bar{\rho}\Delta z)_P^\circ \Big|_{t=0} = \left((\Delta z)_0 \sum_{i=1}^M (X_{i0} \rho_{i0}) \right)_P \quad (26)$$

$$(\bar{\rho}Y_i\Delta z)_P^\circ \Big|_{t=0} = (\bar{\rho}\Delta z)_P^\circ \Big|_{t=0} (Y_{i0})_P \quad (27)$$

$$T_P^\circ(z) \Big|_{t=0} = T_0 \quad \Rightarrow \quad \bar{h}_P^\circ \Big|_{t=0} = \sum_{i=1}^M (Y_{i0} h_{i0})_P \quad (28)$$

$$Y_j^\circ \Big|_{t=0} = Y_{j0} \quad (29)$$

$$P^\circ \Big|_{t=0} = P_\infty \quad (30)$$

In Eqs. 26 and 27, X_{i0} and Y_{i0} are 1.0 for wet wood and 0.0 for all other condensed-phase species. T_0 in Eq. 28 is taken as 300 K. The initial gaseous mass fractions (Eq. 29) are 1.0 for thermal pyrolysate and 0.0 for all other gaseous species. The ambient pressure (Eq. 30) is 101300 Pa.

No boundary conditions are needed for the condensed phase species or mass conservation equations because the condensed phase species and mass conservation equations in each cell reduce to first order transient ordinary differential equations with source terms attributed to species formation and destruction, i.e. there are no convective or diffusive terms in Eqs. 1 and 2.

The boundary conditions on the condensed phase energy equation are:

$$-\bar{k} \frac{\partial T}{\partial z} \Big|_{z=0} = \varepsilon \dot{q}_e'' - h_c (T|_{z=0} - T_\infty) - \varepsilon \sigma (T^4|_{z=0} - T_\infty^4) \quad (31a)$$

$$-\bar{k} \frac{\partial T}{\partial z} \Big|_{z=\delta} = h_{c\delta} (T|_{z=\delta} - T_\infty) \quad (31b)$$

In Eq. 31, \dot{q}_e'' is the externally-applied radiative heat flux in the experiment being simulated, $h_{c\delta}$ is 10 W/m²-K, T_∞ is 300 K, and h_c is the front-face convective heat transfer coefficient front-face convective heat transfer coefficient. The effect of blowing on the latter is estimated with a Couette approximation [20]:

$$h_c = \frac{\dot{m}_0'' c_{pg}}{\exp(\dot{m}_0'' c_{pg} / h_{c,nb}) - 1} \quad (31c)$$

Here, $h_{c,nb}$ (the front face heat transfer coefficient with no blowing) is 10 W/m²-K, \dot{m}_0'' is the calculated mass flux of gases at the surface, and c_{pg} is 1000 J/kg-K.

The boundary conditions on the pressure evolution equation are such that the pressure at the front-face is set to the ambient value. The pressure gradient at the back face is set to give a zero mass flux (impermeable approximation) per Darcy's law:

$$P|_{z=0} = P_\infty \quad (32a)$$

$$\frac{\partial P}{\partial z} \Big|_{z=\delta} = 0 \quad (32b)$$

Eq. 4 (gas-phase species conservation) requires two boundary conditions for each gaseous species j . The back face ($z = \delta$) is assumed impermeable so there is no flow of volatiles across the back face:

$$\left. \frac{\partial Y_j}{\partial z} \right|_{z=\delta} = 0 \quad (33a)$$

The diffusive mass flux of gaseous species into or out of the decomposing solid at the front face is approximated using the heat/mass transfer analogy:

$$-\bar{\psi} \rho_g D \left. \frac{\partial Y_j}{\partial z} \right|_{z=0} \approx \frac{h_c}{c_{pg}} \left(Y_j^\infty - Y_j \Big|_{z=0} \right) \quad (33b)$$

Here, Y_j^∞ is the ambient mass fraction of gaseous species j .

3.3 Material property estimation from 40 kW/m² experimental data

Even with the approximations noted in Section 3.1, almost 50 model input parameters (kinetics coefficients, thermophysical properties, etc.) must be determined. Consequently, model input parameters are estimated from the experimental data in two separate steps. First, a genetic algorithm optimization technique [17, 18] is used in conjunction with the experimental data obtained under nitrogen at 40 kW/m² to estimate values of input parameters that do not involve oxygen (oxidative reactions and species formed by oxidative reactions are not considered). Next, these parameters are held constant while the remaining parameters are determined by genetic algorithm optimization from the experimental data obtained in oxidative atmospheres at 40 kW/m². The model input parameters determined by genetic algorithm optimization (used in all calculations reported in this paper) are listed in Tables 1 through 5.

In the first stage of the model input parameter estimation process (40 kW/m², nitrogen) only heterogeneous reactions that do not involve oxygen (Equations 24.1 and 24.2) affect the calculations. Ash is not formed in the simulations since it is produced

only through an oxidative reaction (Equation 24.4). Similarly, the homogeneous gas-phase reactions both consume oxygen, so they cannot occur in the nitrogen simulations. Any model input parameters associated with these reactions (or the species they produce) have no effect on the nitrogen simulations and are excluded from the first step of the property estimation process.

Fig. 2 compares the measured and calculated temperatures and mass loss rate under nitrogen at 40 kW/m^2 . The calculated surface temperature is slightly higher than the experimental data, but the calculated temperatures at 5 mm and 10 mm match the experimental data very well. The mass loss rate is also well predicted, except that the peak mass loss rate is underpredicted by $\sim 10\%$ and occurs 20 s earlier than in the experiment.

The second stage of the property estimation process involves oxidative atmospheres (10.5% O_2 and 21% O_2 by volume) at 40 kW/m^2 heat flux. The model input parameters determined from the nitrogen experiments are held constant, and genetic algorithm optimization is used to extract the additional parameters from the experimental data at 40 kW/m^2 .

A comparison of the experimental measurements [12] and the optimized model calculations in oxidative environments (40 kW/m^2 heat flux) is given in Figures 3 - 4. Figure 3 is a comparison of the model's temperature calculations with the available experimental data at oxygen concentrations of 10.5% and 21%. The model correctly captures the increase in temperature with ambient oxygen concentration. The combined exothermicity of the heterogeneous and homogeneous reactions causes the temperature to increase as the ambient oxygen concentration is increased. Figure 4 compares the

calculated mass loss rate with the analogous experimental data. Qualitatively, the calculated shape of the mass loss rate curve is similar to the experimental data. Quantitatively, the model calculations match the experimental data well, although the calculated mass loss rate is slightly under-predicted in the later stages of the experiment. This may be due to an under-prediction of the char oxidation rate, or perhaps the onset of another reaction that is not included in the simplified reaction mechanism (Eq. 24).

3.4 Comparison of optimized thermal properties with literature data

In the present study, temperature-dependent specific heat capacity and thermal conductivities are used for each condensed-phase species. Figs. 5 and 6 compare the optimized thermal properties located by the genetic algorithm optimization in the present work with the data of Yang *et al.* [22] as well as thermal property correlations for generic wood from Ref. [13]. In Figs. 5 and 6, generic wood property correlations reported in Ref. [13] are denoted “literature (generic)” and values used by Yang *et al.* [22] to simulate the pyrolysis of white pine are denoted “literature (white pine)”.

In Fig. 5a, the specific heat capacity of the wet wood and dry wood species are compared with the available literature data. It can be seen that the specific heat of dry wood as determined by the genetic algorithm falls between the available literature data. The specific heat capacity of wet wood used in these calculations is within ~20% of the literature data. Fig. 5b shows the specific heat capacity of char as optimized by the genetic algorithm falls between the available literature data.

Fig. 6 gives similar plots for thermal conductivity. It can be seen from Fig. 6a that the thermal conductivity of both wet wood and dry wood optimized by the genetic algorithm

is approximately a factor of two higher than the generic wood literature data, but matches the white pine literature data within ~20%. Interestingly, Fig. 6a shows the opposite trend for wood char. That is, the thermal conductivity optimized by the genetic algorithm matches the generic wood literature data, particularly from 200 °C to 400 °C, but is only 20% to 50% that of the white pine literature data.

3.5 Assessment of model's predictive capabilities at 25 kW/m²

The model is next used to simulate the 25 kW/m² oxidative experiments (which were not used for parameter estimation). Fig. 7 compares the measured and modeled mass loss rate at 25 kW/m² irradiance under nitrogen. It can be seen that the shapes of the curves match reasonably well, but the peak calculated mass loss rate is almost 20% greater than the experimental data and occurs approximately 2 minutes earlier in the model than in the experiment. Discrepancies between the model calculations and the experimental data at this lower heat flux level may be attributed to the simplified reaction mechanism and decomposition kinetics used here. At lower heat flux levels, temperatures are lower and decomposition kinetics play a more significant role than at higher heat flux levels where mass loss rates are controlled primarily by a heat balance. Thus, slight inaccuracies in the decomposition kinetics may lead to larger discrepancies between the model calculations and experimental data at lower heat flux levels.

Figs. 8 and 9 give a comparison of the model calculations and experimental data [12] under oxidative conditions. It can be seen from Fig. 8 that the temperature calculated at five different locations in the decomposing pine slab is usually within ~50 °C of the experimental data for the duration of the experiment. When one considers the uncertainty

in the experimental measurements, this is considered a good fit. A comparison of the measured and modeled mass loss rates (25 kW/m², 10.5% O₂, and 21% O₂) is shown in Fig. 9. The shape of the curve is well-predicted by the model, and the calculated mass loss rate matches the experimental data within ~20% for the duration of the experiments. Again, when one considers the experimental uncertainty and the complexity of the problem, this is considered a good fit.

4. Discussion

The preceding modeling results are encouraging, but at the same time it is evident that there is still room for improvement. This modeling is one of the most comprehensive attempts at simulating wood slab pyrolysis/oxidation for fire applications that has been conducted. Particularly novel is the treatment of the oxidative exothermic reactions, which are accounted for by simulating diffusion of ambient oxygen into the decomposing solid and allowing this oxygen to participate in reactions.

The present simulations include both heterogeneous and homogeneous oxidative reactions, but char oxidation is conventionally viewed as a heterogeneous process. Consequently, it is not clear whether the homogeneous reactions included in the present simulations occur in reality. The effect of these homogeneous reactions on the simulation results was assessed by running calculations with only heterogeneous reactions, only homogeneous reactions, both types of reactions, and neither type of reaction. The results, shown in Fig. 10, are particularly interesting. Comparing the surface temperature in Fig. 10a for the case where both types of reactions occur with the case where only

heterogeneous reactions occur, it can be seen that the homogeneous reactions start to have an effect as the surface temperature approaches 600 °C.

In order to determine whether or not it is feasible that homogeneous gas phase reactions could really start to have an appreciable effect at temperatures near 600 °C, the characteristic time scale of homogeneous gas phase combustion reactions must be compared with the gas phase residence time in the hot char layer. If these time scales are of the same order of magnitude, it is conceivable that homogeneous gas phase combustion reactions could occur as combustible volatiles generated in-depth flow through the hot char layer and react with oxygen that is diffusing inward from the ambient. The order of magnitude of the volatiles' velocity near the surface is ~10 mm/s. Consequently, the residence time in the char layer, assuming it has a thickness of 5 mm, is approximately 0.5 s. Although low-temperature gas phase combustion chemistry is not all that well understood, experimental data [21] for the spontaneous ignition delay time of a lean propane/air premixture at 670 °C (the lowest temperature at which data were reported) is approximately 0.2 s. Thus, at temperatures above 600 °C, the gas phase combustion time scale could approach the residence time in a heated char layer. Consequently, it seems plausible that in oxidative environments, homogenous gas phase reactions could occur inside the pores or voids of a radiatively heated solid and contribute to the overall heat release. However, no firm conclusions can be drawn at this point, and future work in this area is encouraged to help unravel the physical mechanism of oxidative pyrolysis, particularly whether or not homogeneous gas-phase reactions occur.

The present simulations include a simple Couette model for blowing (see Eq. 31c) that, while probably better than not accounting for blowing at all, may not accurately

represent oxygen diffusion through the natural convection boundary layer in the experiments. The calculated surface temperature and mass loss rate for the 21% O₂ case are shown in Fig. 11 with and without blowing enabled. It can be seen that the surface temperature is higher when blowing is disabled due to greater diffusion of oxygen to the surface. Blowing also has an appreciable effect on the calculated peak mass loss rate. Boonme and Quintiere [9] used the classical stagnant layer model (sometimes called the Stefan problem) to account for the effect of blowing through a Spalding mass transfer number (*B* number).

5. Concluding remarks

A model for the oxidative pyrolysis of wood is presented and demonstrated by simulating the nonflaming gasification of white pine slabs irradiated at 25 kW/m² and 40 kW/m² in atmospheres having 0% O₂, 10.5% O₂, and 21% O₂ by volume (balance nitrogen). Diffusion of gaseous oxygen from the ambient into the porous char layer and its effect on oxidative reactions occurring within the decomposing solid is explicitly modeled. Both heterogeneous (gas/solid) and homogeneous (gas/gas) oxidative reactions are considered. The model calculations are compared to experimental data [12] for mass loss rate, surface temperature, and in-depth temperature with generally good agreement.

Due to the relatively large number of species and reactions included in the modeling approach (four condensed-phase species, seven gas-phase species, four heterogeneous reactions, and two homogeneous reactions) almost 50 model parameters (thermal properties, reaction coefficients, etc.) must be determined. A previously developed

genetic algorithm optimization method [17, 18] is used to extract the required input parameters from available experimental data.

Although there is a dearth of literature data for white pine against which the optimized model input parameters can be compared, literature data were located for temperature dependent specific heat capacity and thermal conductivity (generic wood properties [13] and an earlier pyrolysis modeling study of white pine [22]). It was found that the specific heat capacity for wet wood, dry wood, and char falls between literature values for generic wood and specific data for white pine. However, the optimized values of thermal conductivity for wet wood and dry wood are slightly greater than analogous literature data. The thermal conductivity of char is close to one literature value, but it is considerably lower than another literature value. Although no firm conclusions can be drawn, it is felt that the optimized model input parameters located by the genetic algorithm can be treated as material properties, meaning that they should be independent of environmental conditions (applied heat flux, oxygen concentration, etc.). More work is needed to confirm or refute this idea.

A novel feature of the model is that it includes the capability to automatically adjust to changes in environmental conditions (in particular, reduction in the oxygen concentration that a surface feels due to blowing, immersion in an oxygen-vitiated upper layer, or the presence of a nearby diffusion flame). Therefore, this model is adequate for application as a boundary condition in coupled simulations of flame spread and fire growth and future work is planned in this area.

Acknowledgments

This work was supported by NASA Glenn Research Center under Grant NNC-05GA02G. The first author would also like to thank NASA for support under the Graduate Student Researcher Program, Grant NNC-04HA08H, sponsored by NASA Glenn Research Center.

References

- [1] T. Hirata, T. Kashiwagi, J.E. Brown, *Macromolecules* 18 (1985) 1410-1418.
- [2] J. Hayashi, T. Nakahara, K. Kusakabe, S. Morooka, *Fuel Process. Technol.* 55 (1998) 265-275.
- [3] J. Ratha, M.G. Wolfingera, G. Steinera, G. Krammera, F. Barontinib, V. Cozzanib, *Fuel* 82 (2003) 81–91.
- [4] I. Aracil, R. Font, J.A. Conesa, *J. Anal. Appl. Pyrolysis* 74 (2005) 215–223.
- [5] J. Molto, R. Font, J.A. Conesa, *J. Anal. Appl. Pyrolysis* 79 (2007) 289–296.
- [6] J.A. Esfahani, *Combust. Sci. Technol.* 174 (2002) 183-198.
- [7] J.A. Esfahani, M.B. Ayani, M.B. Shirin, *Iranian J. Sci. Technol., Trans. B, Eng.* 29 B2 (2005) 207-218.
- [8] D.K. Shen, M.X. Fang, Z.Y. Luo, K.F. Cen, *Fire Safety J.* 42 (2007) 210-217.
- [9] N. Boonme, J.G. Quintiere, *Proc. Combust. Inst.* 30 (2005) 2303-2310.
- [10] W.G. Weng, Y. Hasemi, W.C. Fan, *Combust. Flame* 145 (2006) 723-729.
- [11] T.J. Ohlemiller, T. Kashiwagi, K. Werner, *Combust. Flame* 69 (1987) 155-170.
- [12] T. Kashiwagi, T.J. Ohlemiller, K. Werner, *Combust. Flame* 69 (1987) 331-345.

- [13] C.W. Lautenberger, A Generalized Pyrolysis Model for Combustible Solids. PhD dissertation, Department of Mechanical Engineering, University of California, Berkeley, Berkeley, CA, 2007.
- [14] C.W. Lautenberger, A.C. Fernandez-Pello, A generalized pyrolysis model for combustible solids, submitted to *Fire Safety Journal* November 2007.
- [15] R.B. Bird, W.E. Stewart, E.N. Lightfoot, Transport Phenomena, New York, John Wiley & Sons, 1960.
- [16] S.V. Patankar, Numerical Heat Transfer and Fluid Flow, New York, Hemisphere Publishing Corporation, 1980.
- [17] C. Lautenberger, G. Rein, A.C. Fernandez-Pello, *Fire Safety J.* 41 (2006) 204-214.
- [18] G. Rein, C. Lautenberger, A.C. Fernandez-Pello, J.L. Torero, D.L. Urban, *Combust. Flame* 146 (2006) 95-108.
- [19] A. Atreya, *Philosophical Trans. Royal Soc. A: Math., Physical, Eng. Sci.* 356 (1998) 2787-2813.
- [20] A.F. Mills, Mass Transfer, Upper Saddle River, NJ, Prentice Hall, 2001, pg. 161.
- [21] G. Freeman, A.H. Lefebvre, *Combust. Flame* 58 (1984) 153-162.
- [22] L. Yang, X. Chen, X. Zhou, W. Fan, *Int. J. Eng. Sci.* 40 (2002) 1011-1021.

List of Figures

Figure 1. Experimentally observed [12] effect of oxygen concentration on the surface temperature and mass loss rate of white pine irradiated at 40 kW/m².

Figure 2. Comparison of model calculations using optimized input parameters and experimental data for pyrolysis of white pine at 40 kW/m² irradiance in nitrogen.

Figure 3. Comparison of experimentally measured [12] and modeled temperatures at several depths below the surface of white pine irradiated at 40 kW/m².

Figure 4. Comparison of experimentally measured [12] and modeled mass loss rate of white pine at 40 kW/m² irradiance.

Figure 5. Comparison of temperature-dependent specific heat capacity optimized by genetic algorithm with literature data.

Figure 6. Comparison of temperature-dependent thermal conductivity optimized by genetic algorithm with literature data.

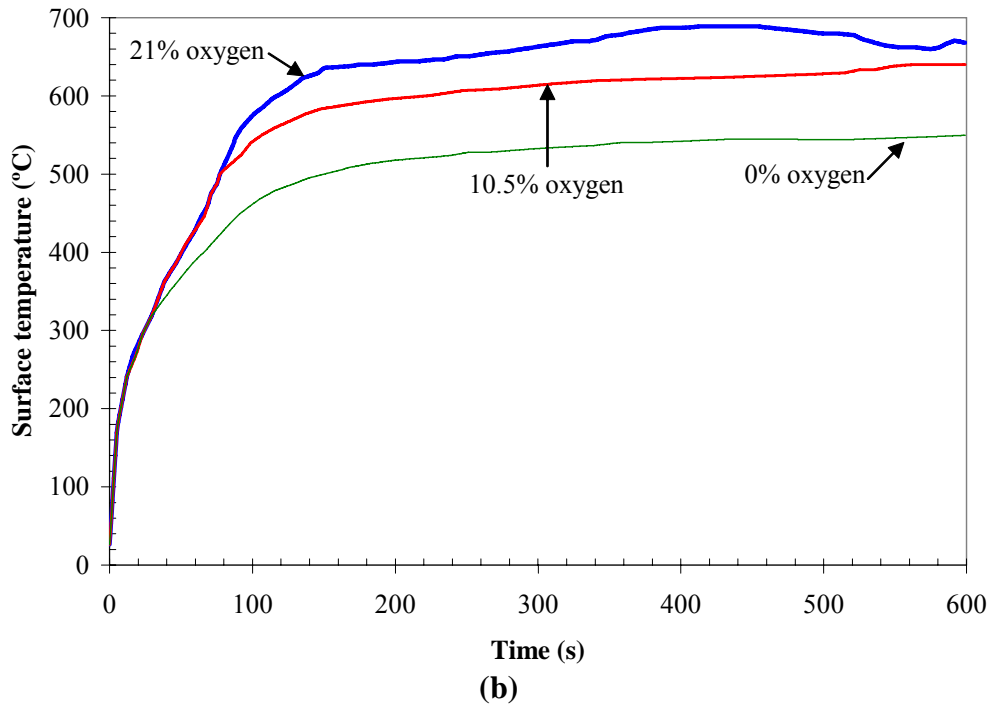
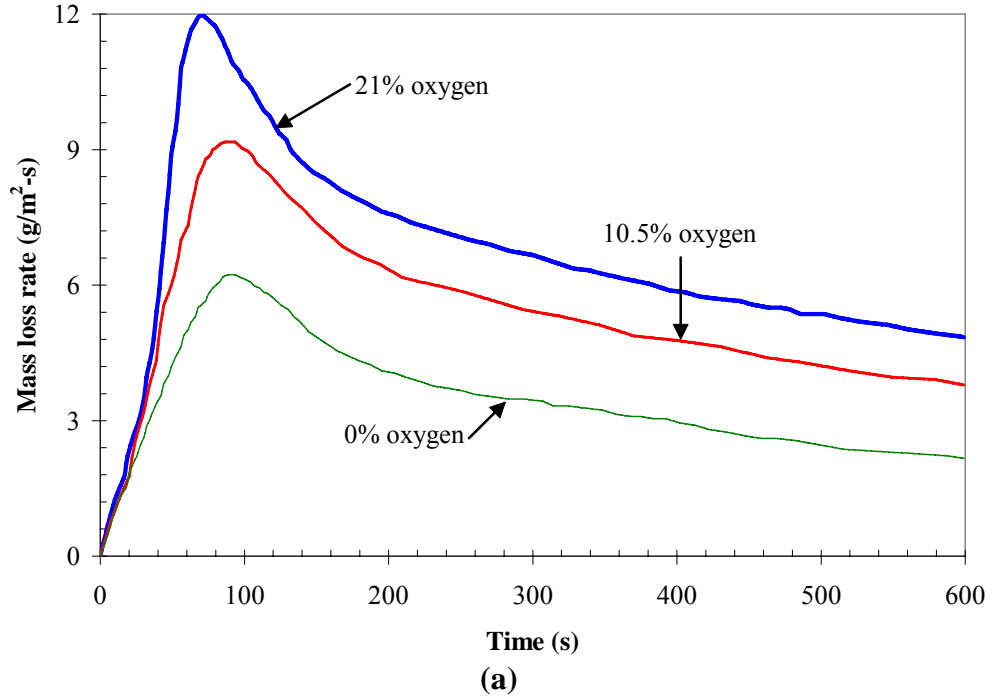
Figure 7. Comparison of modeled mass loss rate and experimental data for pyrolysis of white pine at 25 kW/m² irradiance in nitrogen.

Figure 8. Comparison of experimentally measured [12] and modeled temperatures at several depths below the surface of white pine irradiated at 25 kW/m² in 10.5% O₂ atmosphere.

Figure 9. Comparison of experimentally measured [12] and modeled mass loss rate of white pine at 25 kW/m² irradiance.

Figure 10. Effect of heterogeneous and homogeneous reactions on the oxidative pyrolysis of white pine at 40 kW/m² irradiance and 21% O₂. Text in figures indicates reactions included in simulations.

Figure 11. Effect of blowing on calculated mass loss rate of white pine at 40 kW/m² irradiance and 21% O₂.



**Figure 1. Experimentally observed [12] effect of oxygen concentration on the surface temperature and mass loss rate of white pine irradiated at 40 kW/m².
a) Mass loss rate; b) Temperature.**

Figure 1

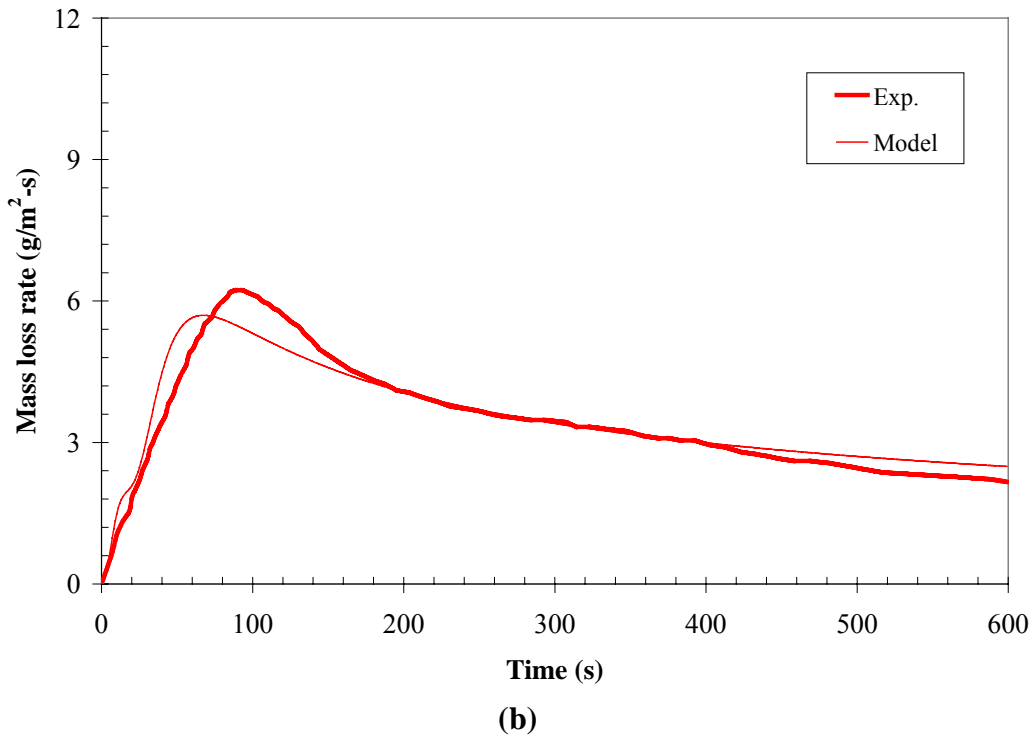
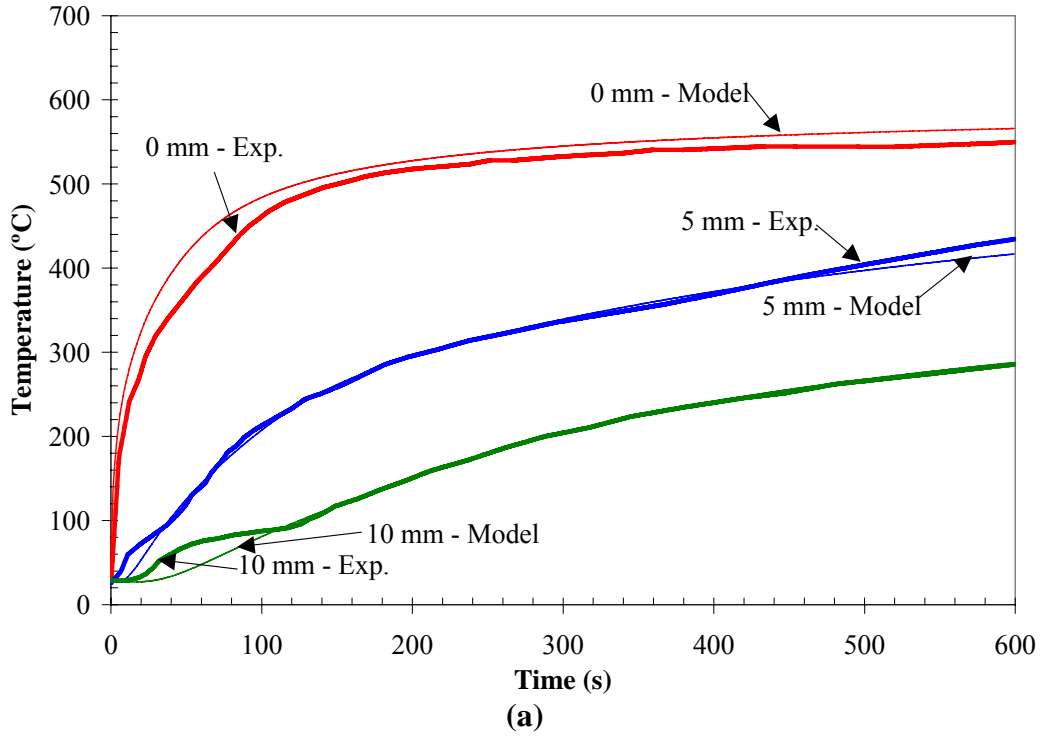


Figure 2. Comparison of model calculations using optimized input parameters and experimental data for pyrolysis of white pine at 40 kW/m² irradiance in nitrogen. (a) Temperature; (b) Mass loss rate.

Figure 2

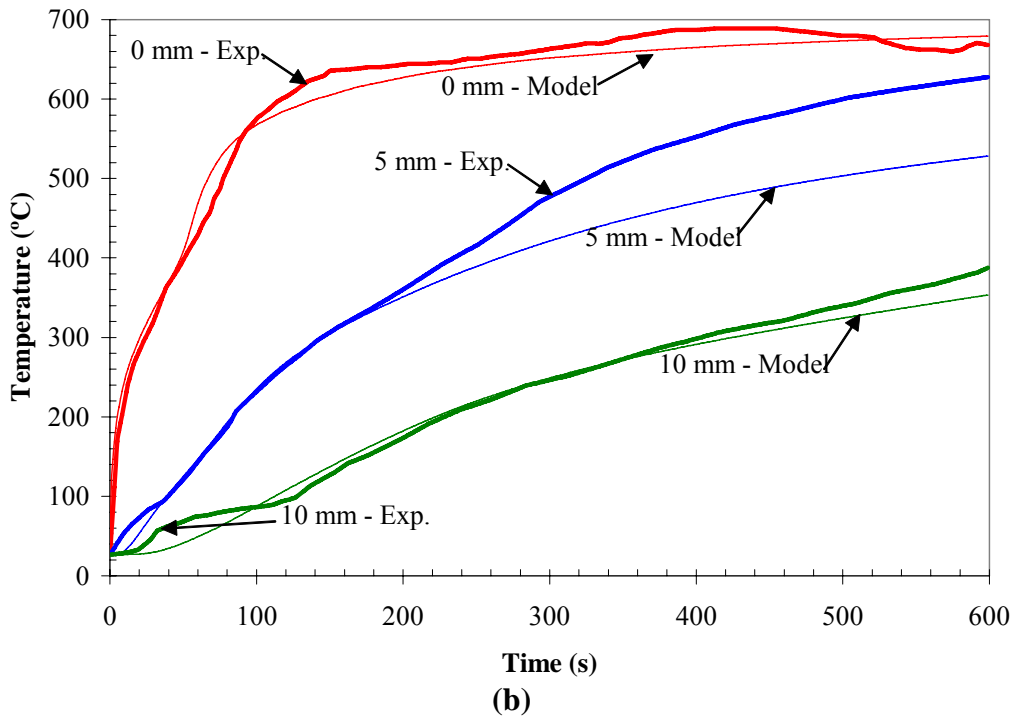
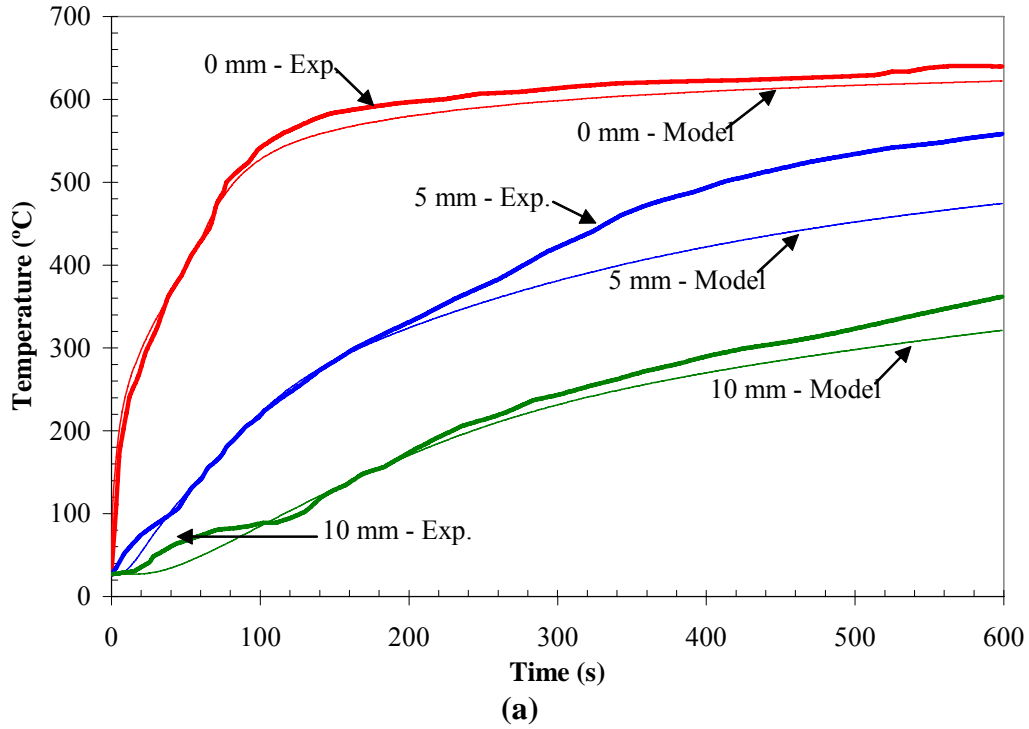
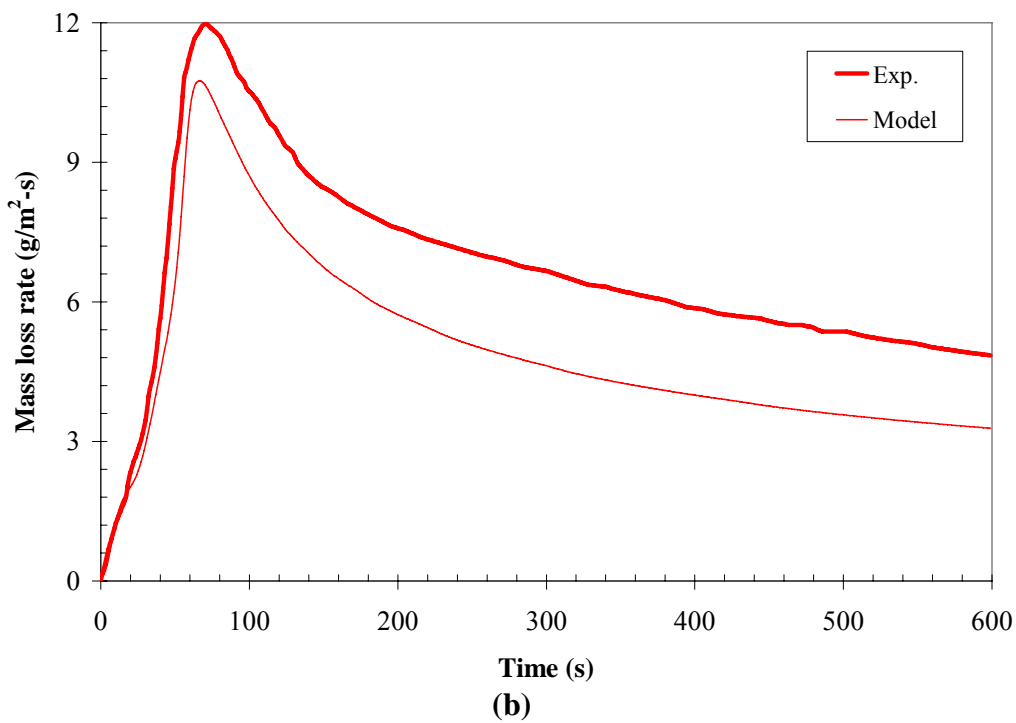
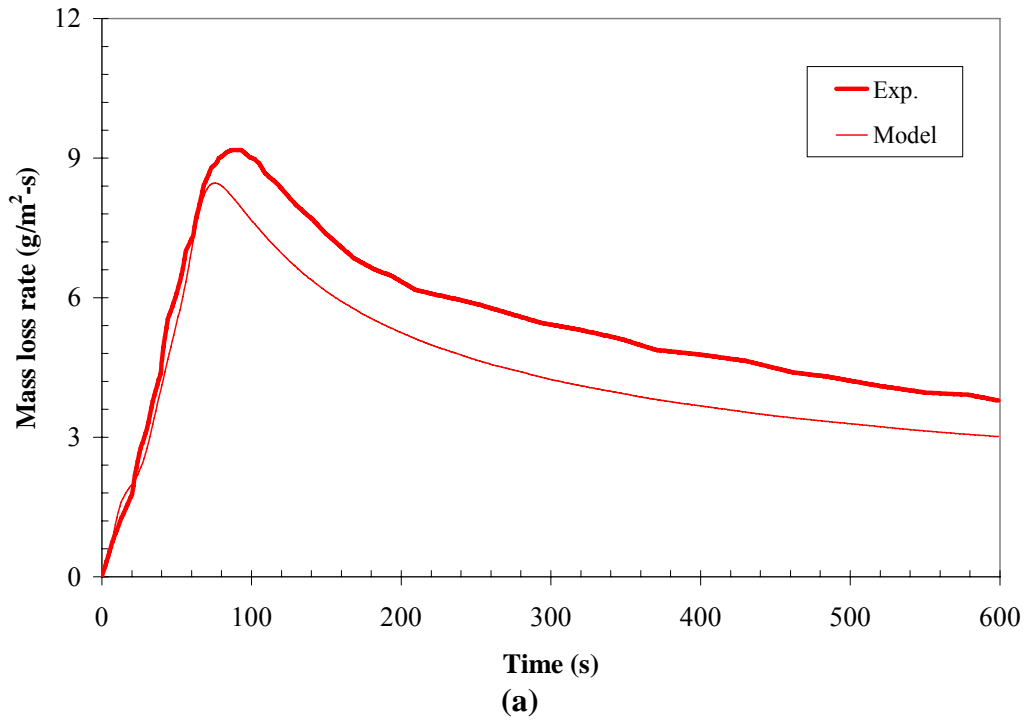
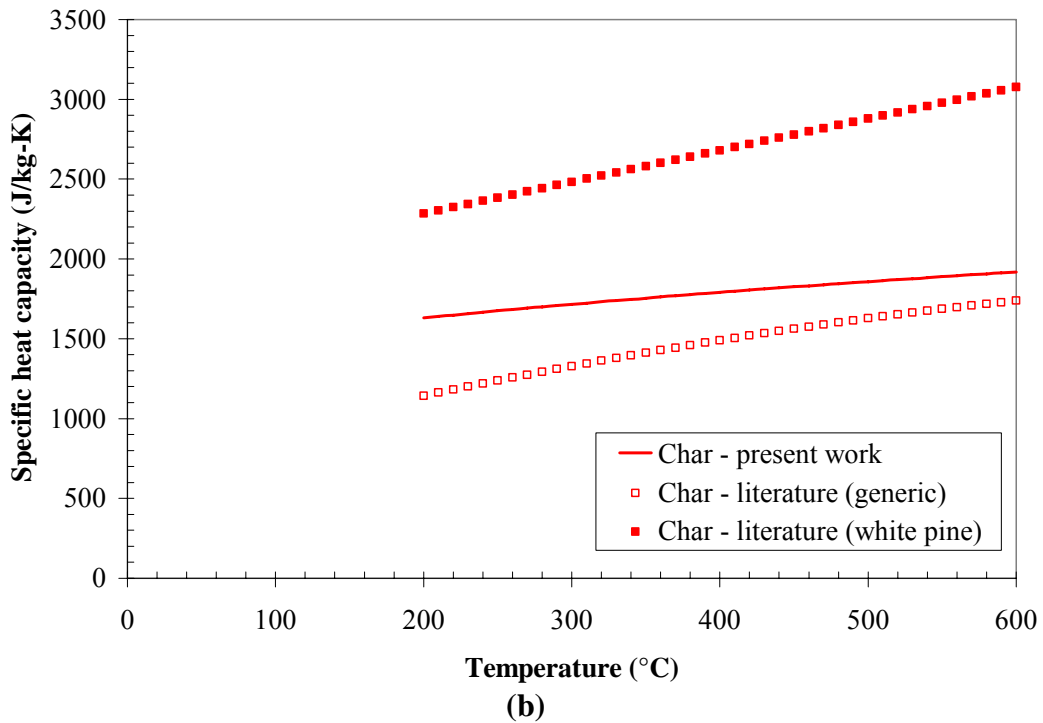
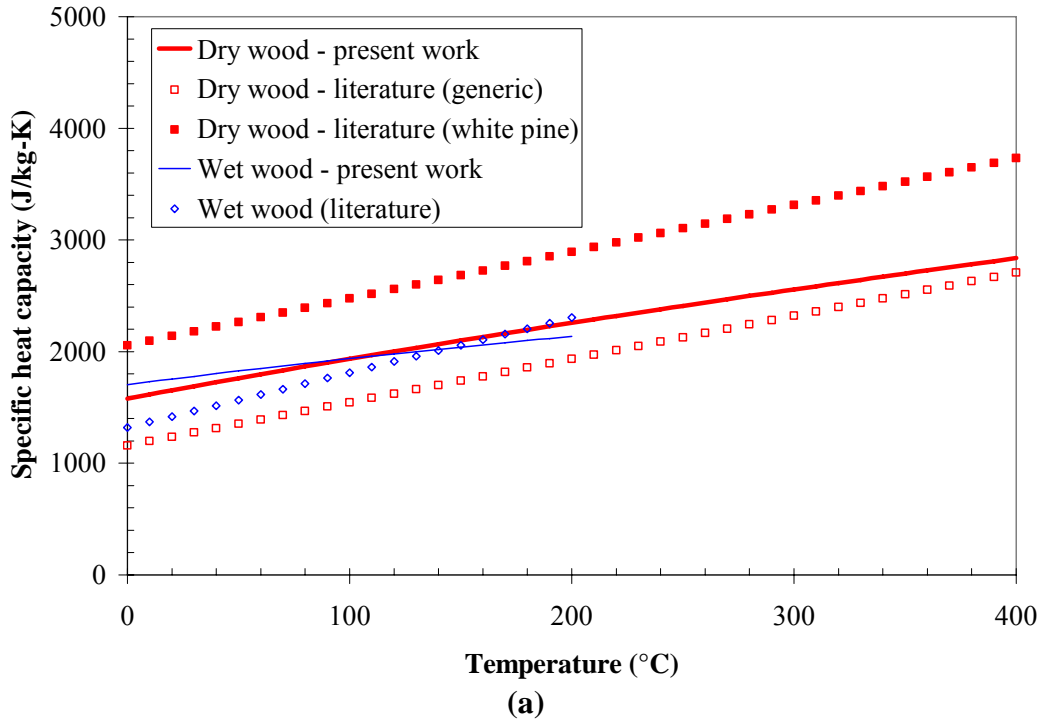


Figure 3. Comparison of experimentally measured [12] and modeled temperatures at several depths below the surface of white pine irradiated at 40 kW/m^2 . a) 10.5% O_2 atmosphere; b) 21% O_2 atmosphere.

Figure 3



**Figure 4. Comparison of experimentally measured [12] and modeled mass loss rate of white pine at 40 kW/m² irradiance.
a) 10.5% O₂ atmosphere; b) 21% O₂ atmosphere.**



**Figure 5. Comparison of temperature-dependent specific heat capacity optimized by genetic algorithm with literature data.
a) Virgin wood; b) Char.**

Figure 5

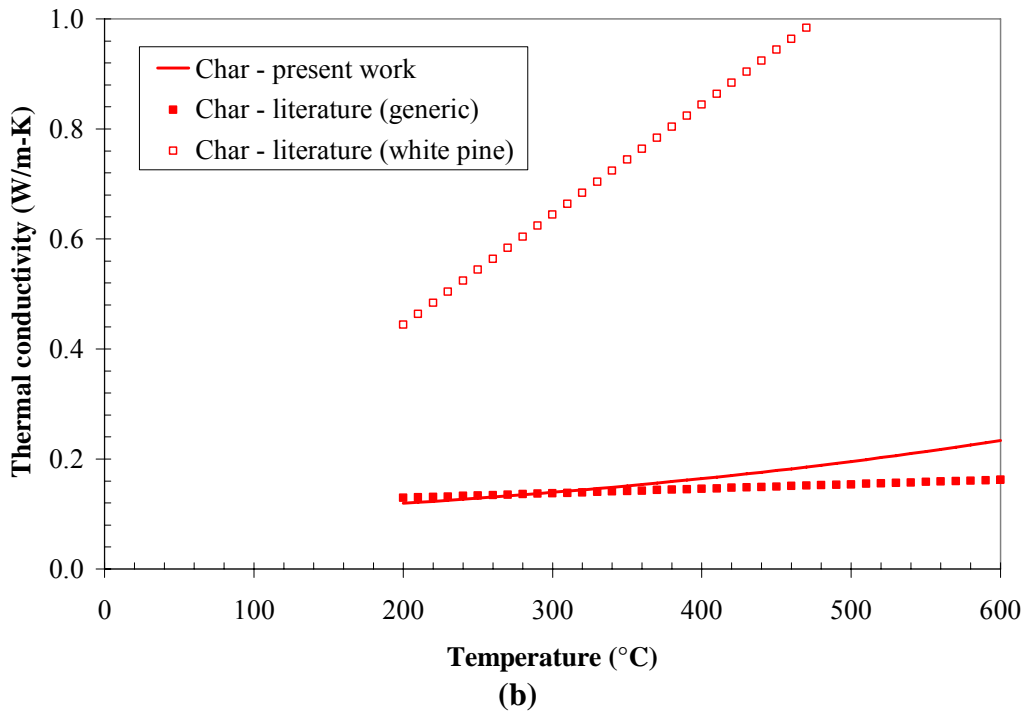
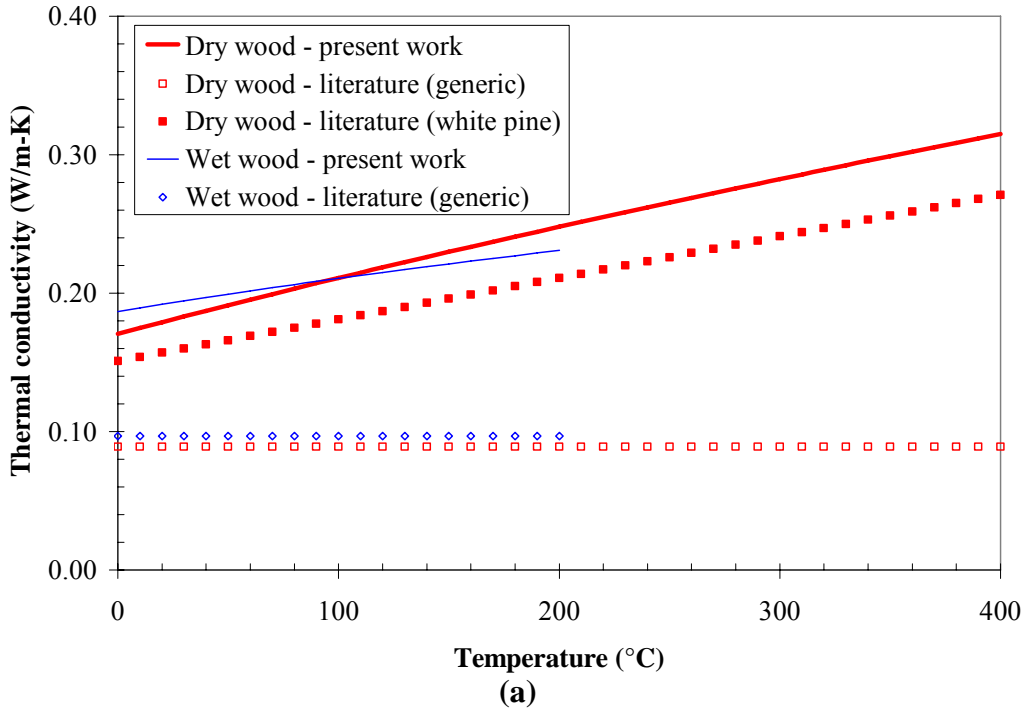


**Figure 6. Comparison of temperature-dependent thermal conductivity optimized by genetic algorithm with literature data.
a) Virgin wood; b) Char.**

Figure 6

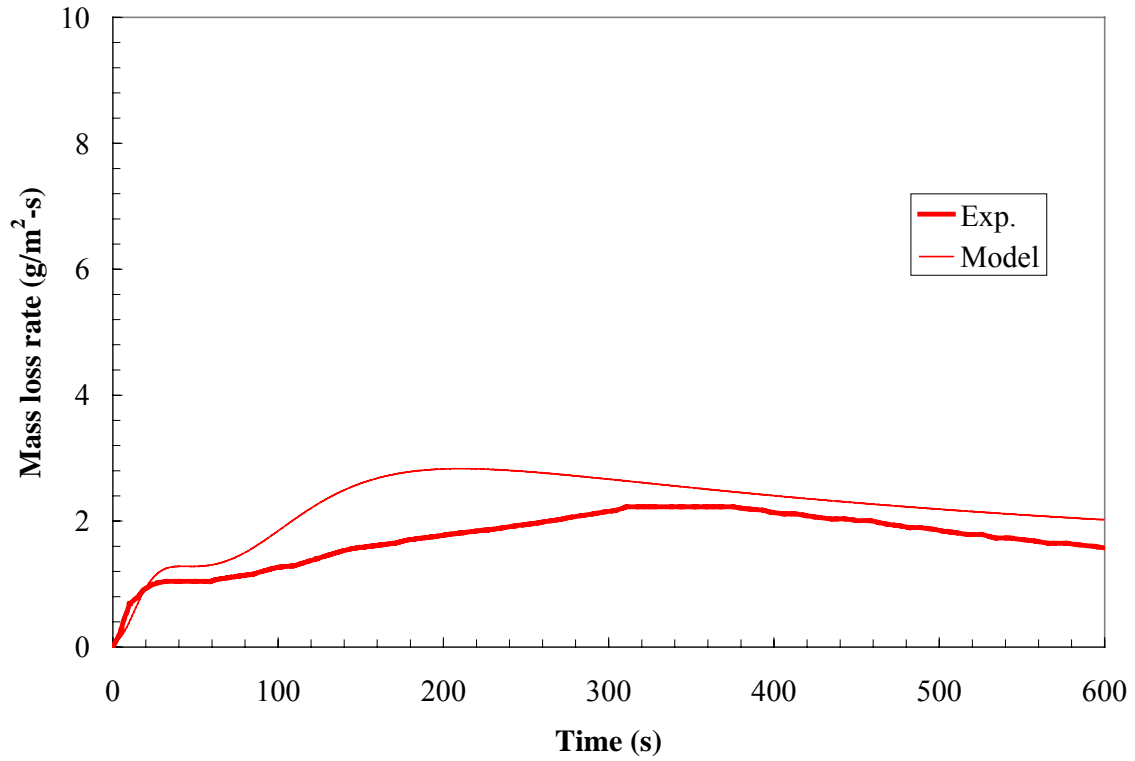


Figure 7. Comparison of modeled mass loss rate and experimental data for pyrolysis of white pine at 25 kW/m² irradiance in nitrogen.

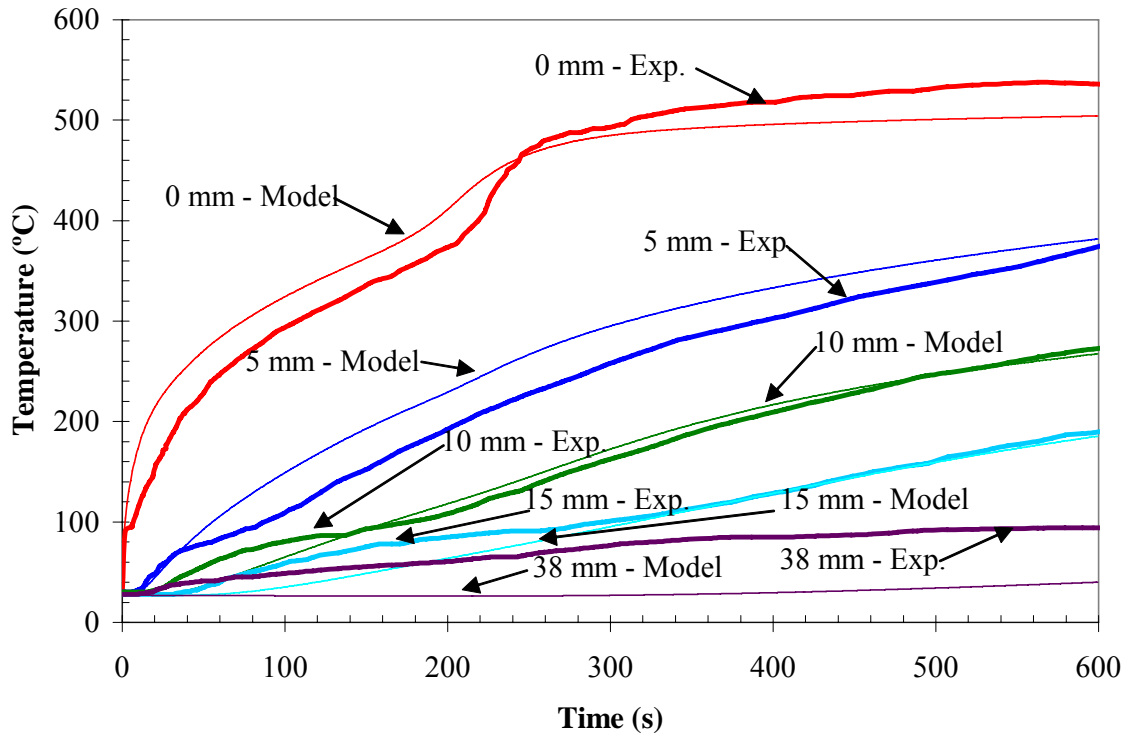


Figure 8. Comparison of experimentally measured [12] and modeled temperatures at several depths below the surface of white pine irradiated at 25 kW/m² in 10.5% O₂ atmosphere.

Figure 8

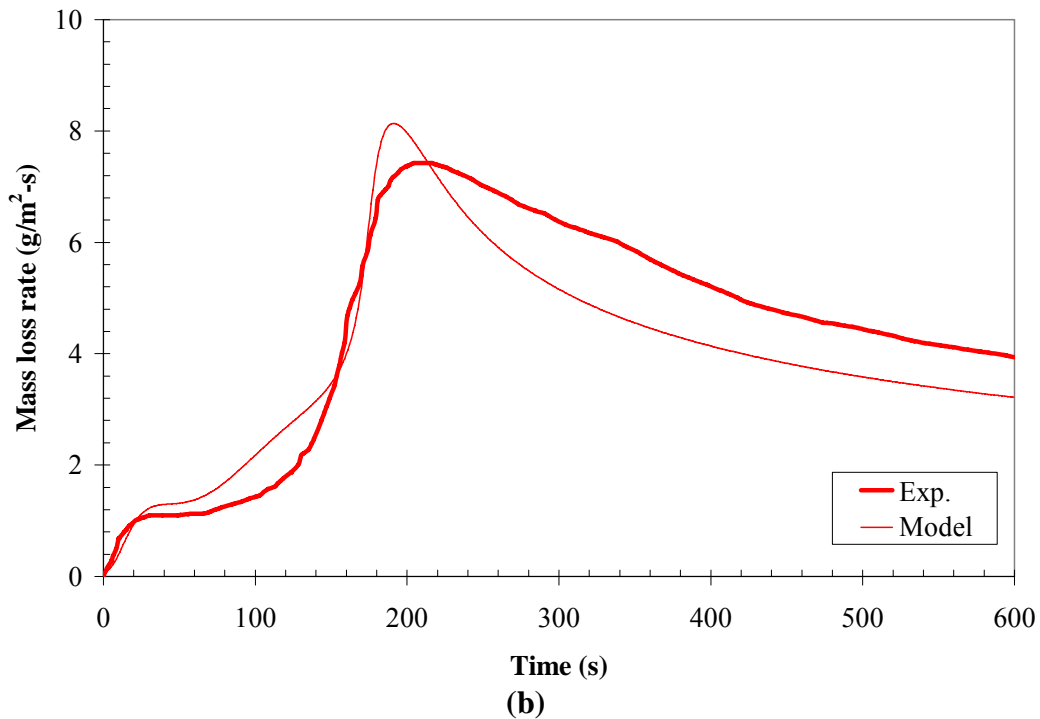
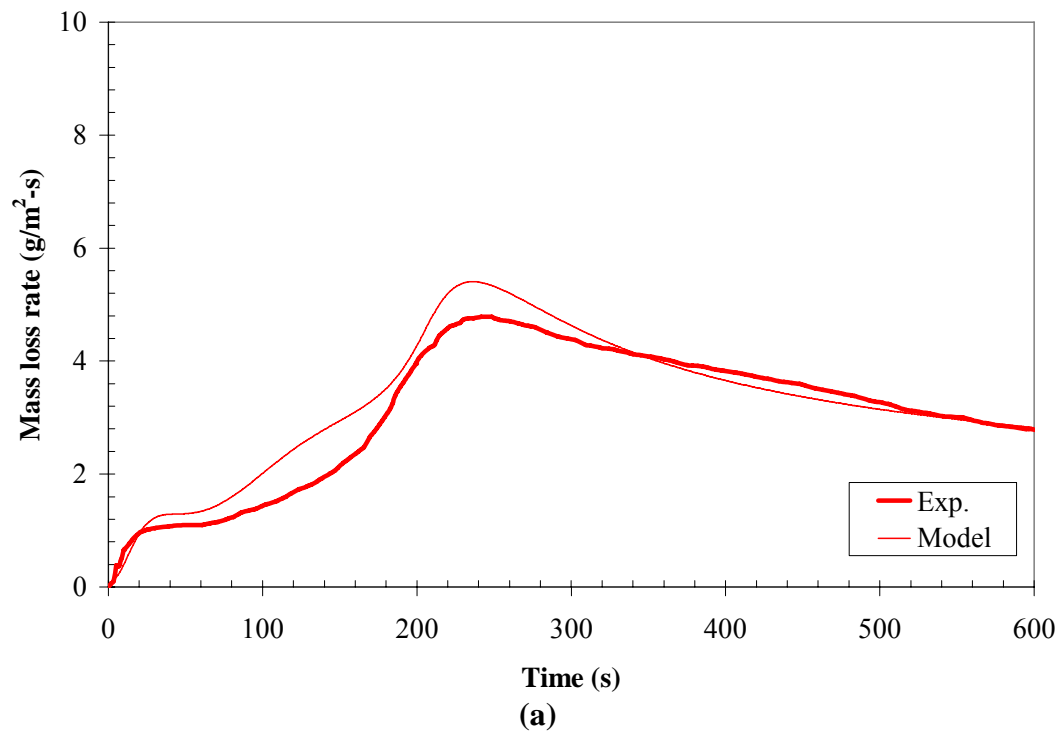


Figure 9. Comparison of experimentally measured [12] and modeled mass loss rate of white pine at 25 kW/m² irradiance. a) 10.5% O₂ atmosphere; b) 21% O₂ atmosphere.

Figure 9

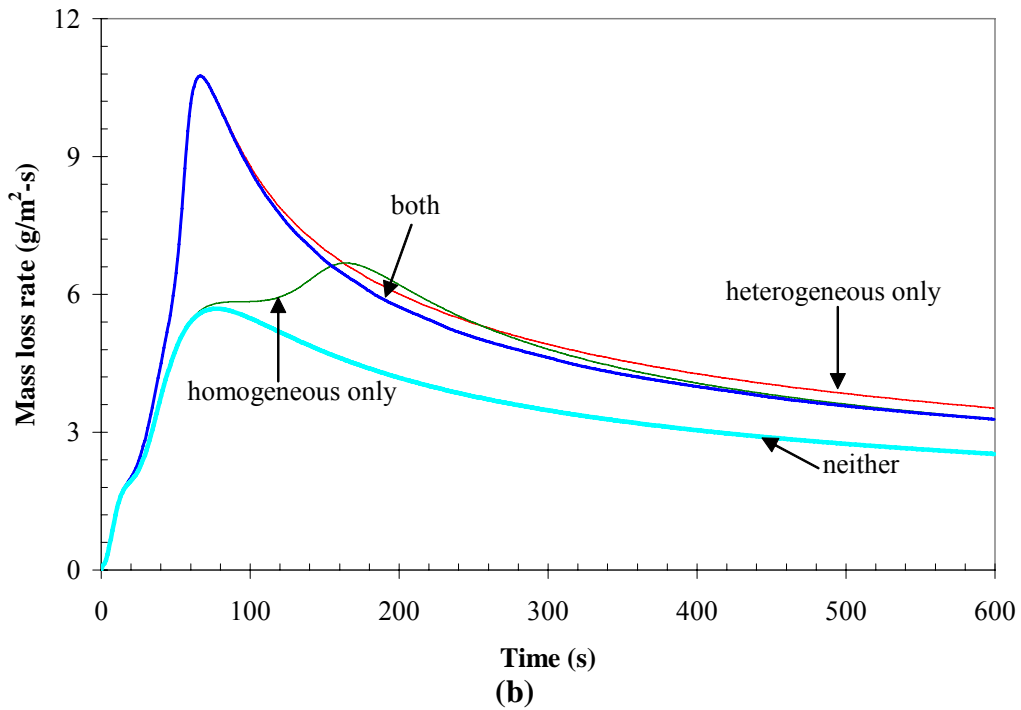
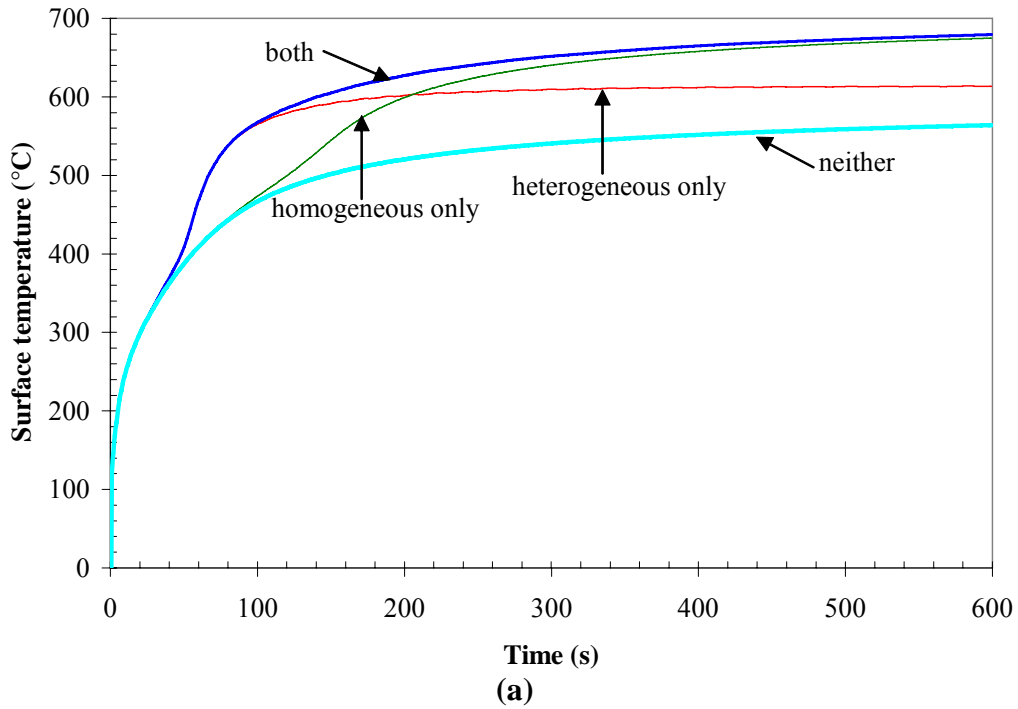
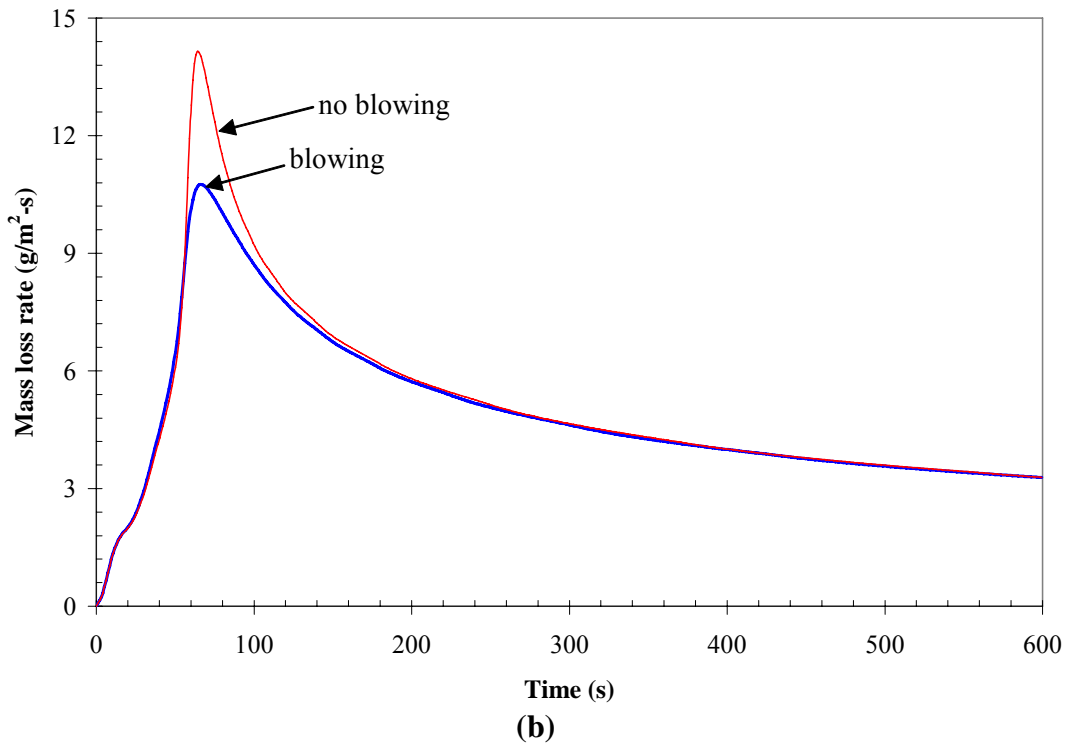
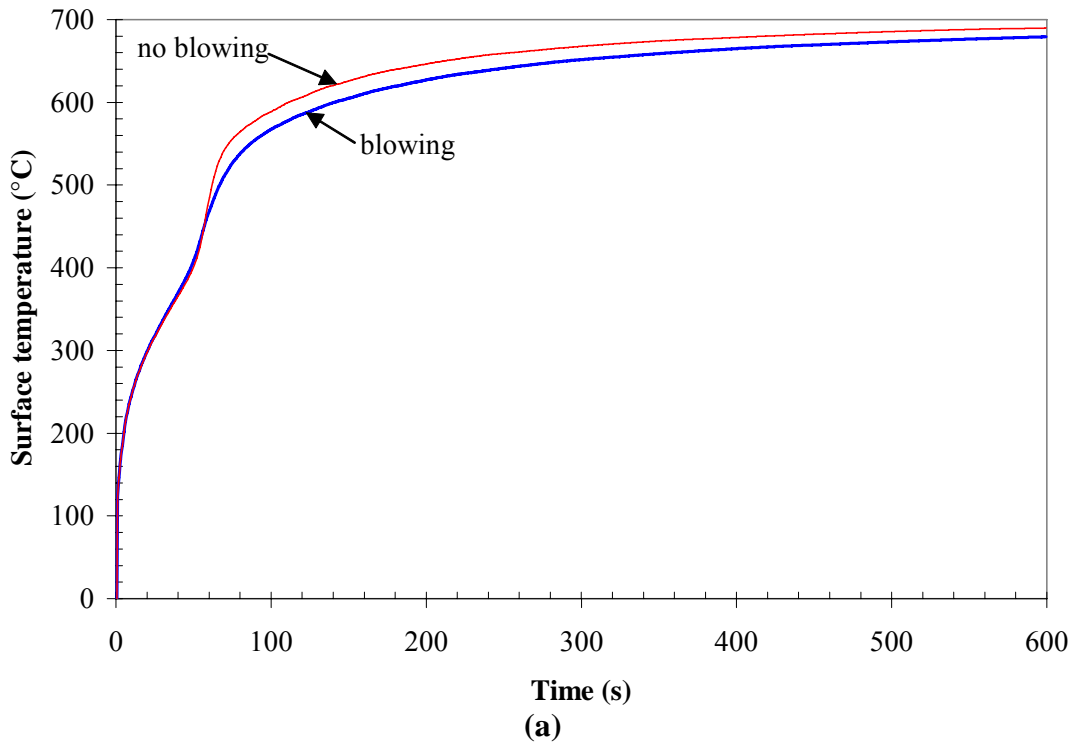


Figure 10. Effect of heterogeneous and homogeneous reactions on the oxidative pyrolysis of white pine at 40 kW/m² irradiance and 21% O₂. Text in figures indicates reactions included in simulations. a) Surface temperature; b) Mass loss rate.

Figure 10



**Figure 11. Effect of blowing on calculated mass loss rate of white pine at 40 kW/m² irradiance and 21% O₂.
a) Surface temperature; b) Mass loss rate.**

Figure 11

List of Tables

Table 1. Condensed phase parameters for white pine simulations.

Table 2. Reaction parameters for white pine simulations.

Table 3. Gaseous yields for white pine simulations.

Table 4. Homogeneous gaseous reaction parameters for white pine simulations.

Table 5. Homogeneous gaseous yields for white pine simulations. Only nonzero yields are shown.

Table 1. Condensed phase parameters for white pine simulations.

i	Name	k_0 (W/m-K)	n_k (-)	ρ_0 (kg/m ³)	n_ρ (-)	c_0 (J/kg-K)	n_c (-)	ε (-)	γ (m)	ρ_{s0} (kg/m ³)
1	wet wood	0.194	0.386	380	0	1772	0.411	0.755	0	380.1
2	dry wood	0.182	0.679	360	0	1680	0.649	0.757	0	380.1
3	char	0.089	0.304	88.5	0	1445	0.266	0.973	2.9×10^{-3}	380.1
4	ash	0.079	0.157	5.7	0	1229	0.226	0.973	7.1×10^{-3}	380.1

Table 1

Table 2. Reaction parameters for white pine simulations.

k	From	To	χ (-)	ΔH_s (J/kg)	ΔH_v (J/kg)	Z (s ⁻¹)	E (kJ/mol)	n (-)	n_{O_2} (-)
1	wet wood	dry wood	1	0	2.41×10^6	4.31×10^3	43.6	1.02	0
2	dry wood	char	1	0	6.74×10^5	3.14×10^9	135.4	5.42	0
3	dry wood	char	1	0	-9.15×10^5	3.14×10^9	126.7	5.42	1.31
4	char	ash	1	0	-3.05×10^7	9.02×10^{13}	192.6	1.51	1.91

Table 2

**Table 3. Gaseous yields for white pine simulations.
Only nonzero yields are shown.**

$j \backslash k$	1	2	3	4
1 (thermal pyrolysate)		1		
2 (nitrogen)				
3 (water vapor)	1			
4 (oxygen)			-0.1	-2.0
5 (oxidative pyrolysate)			1.1	
6 (char oxidation products)				3.0
7 (pyrolysate oxidation products)				

Table 3

Table 4. Homogeneous gaseous reaction parameters for white pine simulations.

k	Reactant 1	Reactant 2	p (-)	q (-)	b (-)	Z	E (kJ/mol)	ΔH (MJ/kg)
1	thermal pyrolysate	oxygen	1.0	1.0	0.0	6.76×10^9	163.2	-1.98×10^7
2	oxidative pyrolysate	oxygen	1.0	1.0	0.0	7.31×10^9	162.2	-1.92×10^7

Table 5. Homogeneous gaseous yields for white pine simulations. Only nonzero yields are shown.

j \ k	1	2
1 (thermal pyrolysate)	-1.0	
2 (nitrogen)		
3 (water vapor)		
4 (oxygen)	-1.6	-1.5
5 (oxidative pyrolysate)		-1.0
6 (char oxidation products)		
7 (pyrolysate oxidation products)	2.6	2.5

Table 5